Supplementary Information for

A class of metal diboride electrocatalysts synthesized by a molten salt-assisted reaction for the hydrogen evolution reaction

Feifan Guo,[a,‡] Yuanyuan Wu,[a,b,‡] Xuan Ai,[a,‡] Hui Chen,[a] Guo-Dong Li,[a] Wei Chen[c] and

Xiaoxin Zou*[a]

[a] State Key Laboratory of Inorganic Synthesis and Preparative Chemistry, International Joint Research Laboratory of Nano-Micro Architecture Chemistry, College of Chemistry, Jilin University, Changchun 130012, P. R. China

[b] Key Laboratory of Preparation and Application of Environmental Friendly Materials (Jilin Normal University), Ministry of Education, Changchun 130103, China

[c] Laboratory of Theoretical and Computational Chemistry, Institute of Theoretical Chemistry, International Joint Research Laboratory of Nano-Micro Architecture Chemistry, Jilin University, Changchun 130023, P. R. China

‡ F. Guo, Y. Wu and X. Ai contributed equally to this work.

1. Experiment Section

1.1 Chemicals Reagents. Sodium chloride (NaCl), potassium chloride (KCl), zirconium dioxide (ZrO_2), hafnium dioxide (HfO_2), dichromium trioxide (Cr_2O_3), molybdenum trioxide (MoO_3), tungsten trioxide (WO_3), nickel oxide (NiO), ruthenium dioxide (RuO_2), Rhenium (Re), amorphous boron (B) and Nafion® perfluorinated resin solution were purchased from Aladdin. Titanium dioxide (TiO_2) and isopropyl alcohol were purchased from Beijing Chemical Works. Vanadium pentoxide (V_2O_5), niobium pentoxide (Nb_2O_5) and tantalum pentoxide (Ta_2O_5) were purchased from Tianjin Guangfu Fine Chemical Research Institute. Manganese bioxide (MnO_2) was purchased from Tianjin Huadong Reagent Factory.

1.2 Synthesis of Transition Metal Diborides (MB_2). The metal diborides were synthetized by boronthermal reduction in molten salts with equal molar ratio (KCl-NaCl). The melting point of molten salt (KCl-NaCl) is about 650 °C. The precursors (metal oxide and boron powder, Table S1) were fully ground for about 15 min as well as the molten salt. The mixture was placed into an Al_2O_3 crucible and then heated at 950 °C or 1000 °C for 1 h in a tubular furnace under Ar atmosphere, the heating rate was 10 °C min^{-1}. After cooling, a block of salt in the crucible was washed three times with warm water of 80 °C to remove the inorganic salts and the by-products B_yO_z. The final sample was washed with ethanol and dried in vacuum drying oven at 80 °C. It is worth noting that the rhenium was used as a raw material for the synthesis of rhenium diborides.

Ni doped WB_2 catalysts are prepared by introducing different molar amounts of nickel oxide (NiO) into the precursor, and the other reaction conditions are the same as those described above.

1.3 Characterizations. The powder X-ray diffraction (XRD) patterns were obtained with a Rigaku D/Max 2550 X-ray diffractometer with Cu Kα radiation (λ = 1.5418 Å). The scanning electron microscope (SEM) images were obtained with a

JEOL JSM 6700F electron microscope. The transmission electron microscope (TEM) images were obtained with a Philips-FEI Tecnai G2S-Twin microscope equipped with a field emission gun operating at 200 kV. The X-ray photoelectron spectroscopy (XPS) was performed on an ESCALAB 250 X-ray photoelectron spectrometer with a monochromatic X-ray source (Al Kα $h\upsilon$ = 1486.6 eV). The specific surface area was obtained useing the Brunauer-Emmett-Teller (BET) method on a Micromeritics ASAP 2020 M system.

1.4 Electrochemical Measurements. The electrochemical measurements were performed in a three-electrode configuration with a CH Instrument (Model 650E). A saturated calomel electrode (SCE) and a carbon rod were used as the reference electrode and as the counter electrode, respectively. The SCE electrode was calibrated according to our previous report,[1] and the calibration result of the SCE electrode was 0.263 V. The relation between the SCE electrode and the reversible hydrogen electrode (RHE) were established in 0.5 M H_2SO_4 solution using the equation: $E_{vs\ RHE} = E_{vs\ SCE} + 0.263$ V. Regarding the preparation method of the working electrode: firstly we took 5 mg of the sample and ultrasonically dispersed it in 300 μL of isopropyl alcohol solution, then took 2 μL of the above solution onto a glassy carbon electrode (GCE), giving a catalyst loading of ~0.46 mg cm^{-2}, and finally dripped coating 2 μL of 0.3 % Nafion solution to protect the film. A scan rate of 1 mV s^{-1} was used for linear sweep voltammetry (LSV) measurements and 85% *iR* correction was performed. The Faradaic efficiency during HER electrocatalysis was determined according to the procedures reported in our previous work. Electrochemical Impedance Spectroscopy was performed under the HER operating conditions.[2] The initial potential at the electrode was set as -0.2 V *vs.* RHE for direct comparison. A sinusoidal voltage with an amplitude of 5 mV and a scanning frequency ranging from 100 kHz to 0.05 Hz were applied to carry out the measurements.

1.5 Estimation of Effective Electrode Surface Area. In order to estimate the effective surface area of electrodes, the electrochemical double-layer capacitance (C_{dl}) was estimated by cyclic voltammograms (CV) for different catalysts under non-

faradaic region in 0.5 M H_2SO_4. Therefore, a series of CV tests were performed at different scan rates (10 mV s^{-1}, 20 mV s^{-1}, 30 mV s^{-1}, *etc.*) over a potential range of 0.1-0.2 V *versus* RHE. All measured current in this region is assumed to be due to double-layer charging. Based on the assumption, the anode (i_a)and cathode current (i_c) differences were plotted as a function of scan rates at 0.15 V *vs.* RHE. The slope of fitted line of the data points, which is equal to twice of C_{dl}. The electrochemically active surface area (ECSA) could be calculated by dividing C_{dl} by a specific capacitance (C_s, 0.035 mF cm^{-2} in 0.5 M H_2SO_4).
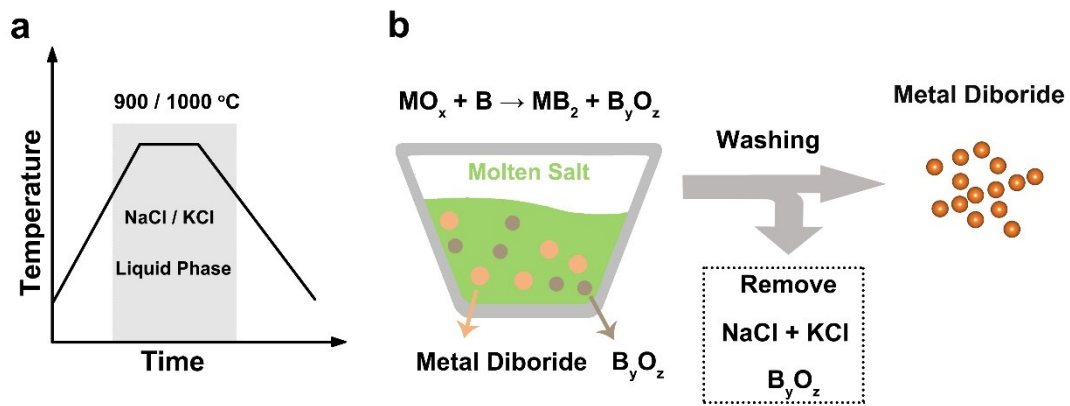
Fig. S1. (a) The reaction temperature between MO_x and B precursors occurs in the liquid phase domain of molten salts. (b) Schematic diagram of the synthesis for metal diborides.

Tab. S1. Specific parameters of chemicals used in experiments corresponding to metal diborides

Metal Diborides	Mass of Metal Oxides	Mass of Boron	Mass of Molten Salt	Temperature / Time
TiB_2	0.240 g	0.130 g	3.700 g	900 °C / 1 h
VB_2	0.364 g	0.195 g	2.793 g	900 °C / 1 h
CrB_2	0.304 g	0.151 g	4.550 g	900 °C / 1 h
MnB_2	0.261 g	0.176 g	4.370 g	900 °C / 1 h
ZrB_2	0.246 g	0.173 g	2.097 g	1000 °C / 1 h
NbB_2	0.266 g	0.097 g	1.816 g	900 °C / 1 h
MoB_2	0.288 g	0.173 g	4.610 g	900 °C / 1 h
HfB_2	0.211 g	0.087 g	1.485 g	1000 °C / 1 h
TaB_2	0.442 g	0.097 g	2.696 g	900 °C / 1 h
WB_2	0.348 g	0.130 g	4.778 g	1000 °C / 1 h
ReB_2[a]	0.372 g	0.087 g	4.584 g	1000 °C / 1 h
RuB_2	0.133 g	0.054 g	1.872 g	900 °C / 1 h

Note: [a] The rhenium was used as a raw material for the synthesis of rhenium diborides.
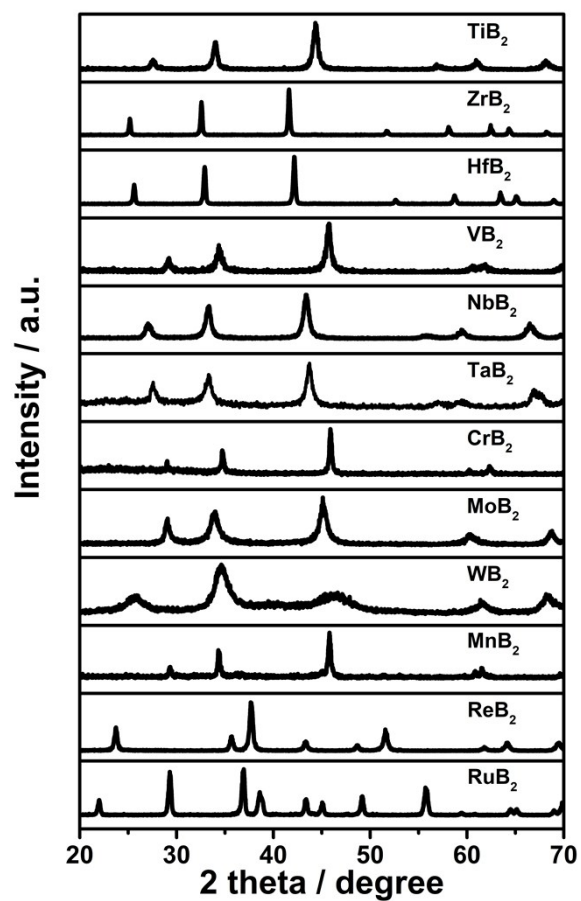
Fig. S2. The powder X-ray diffraction (XRD) patterns of twelve metal diborides.
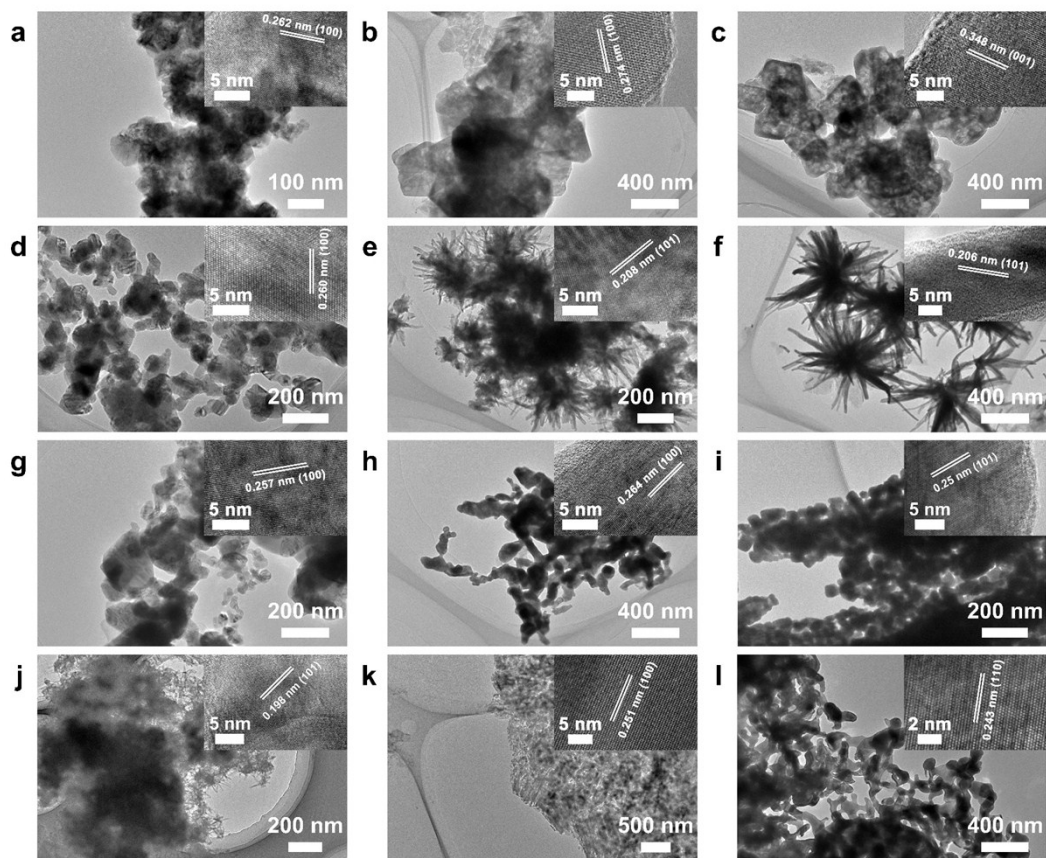
Fig. S3. TEM and HR-TEM (inset) images of twelvel metal diborides. As shown in Fig. S3, the (a) TiB$_2$, (b) ZrB$_2$, (c) HfB$_2$, (d) VB$_2$, (g) CrB$_2$ and (k) ReB$_2$ possess a nanosheet structure. The (e) NbB$_2$, (f) TaB$_2$, and (j) MnB$_2$ have a needle structure. The (h) MoB$_2$, (i) WB$_2$ and (l) RuB$_2$ consist of aggregated nanoparticles.

Tab. S2. The BET surface areas of metal diboride.

Sample	BET Surface Area / $m^2\ g^{-1}$	Sample	BET Surface Area / $m^2\ g^{-1}$
TiB_2	24.8	CrB_2	15.2
ZrB_2	73.7	MoB_2	11.2
HfB_2	69.2	WB_2	15.0
VB_2	15.1	MnB_2	28.2
NbB_2	28.2	ReB_2	4.5
TaB_2	18.5	RuB_2	8.6
		$Ni\text{-}WB_2$	11.0
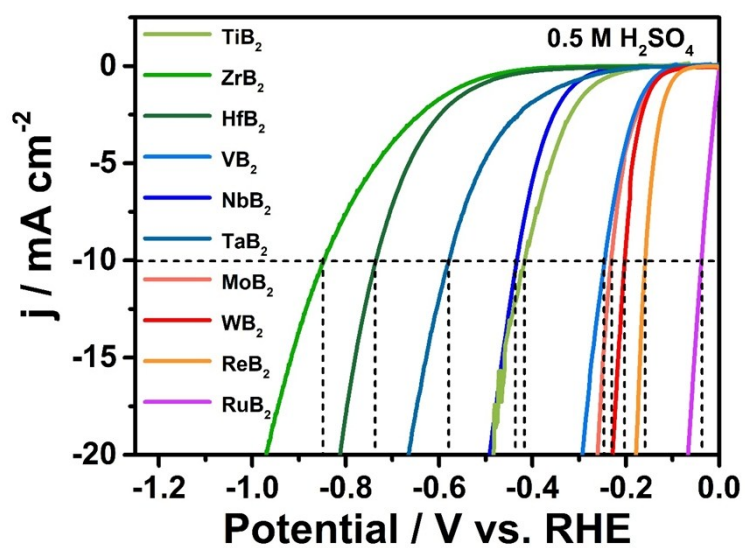
Fig. S4. HER polarization curves of MB_2 (M = Ti, Zr, Hf, V, Nb, Ta, Mo, W, Re, Ru) in 0.5 M H_2SO_4 solution with 85% iR-compensations.
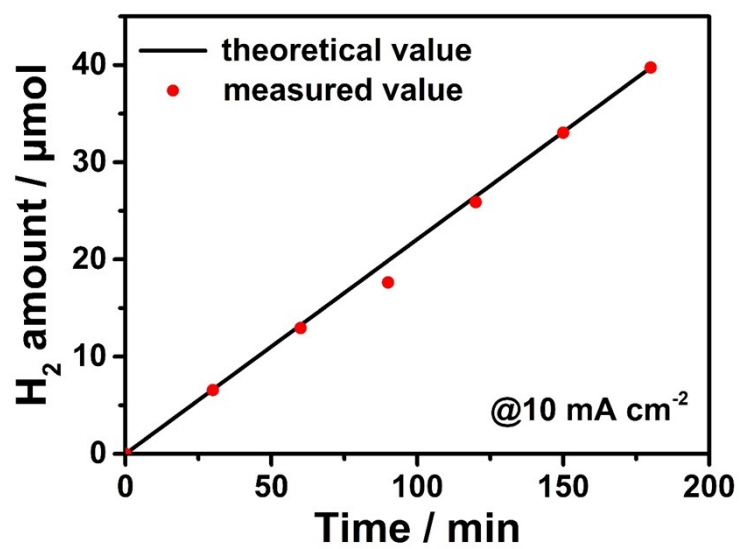
Fig. S5. Electrocatalytic efficiency of WB_2 for HER at a current density of 10 mA cm^{-2} in 0.5 M H_2SO_4.
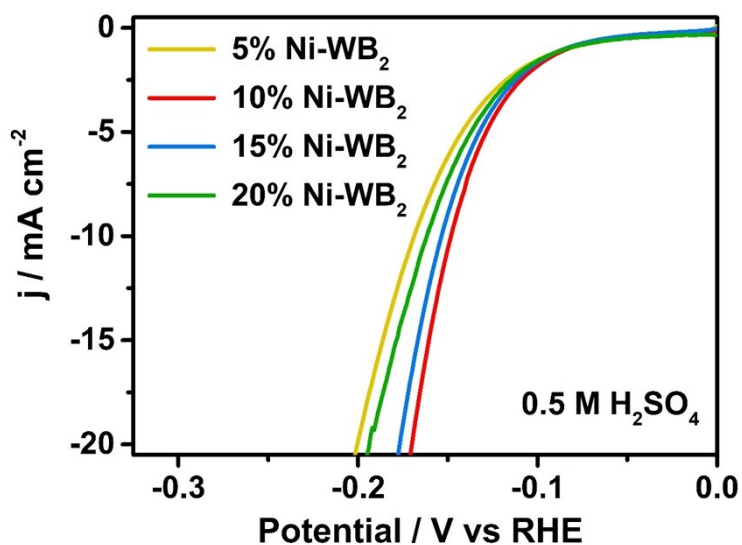
Fig. S6. Linear sweep voltammetry (LSV) curves toward the HER in a 0.5 M H_2SO_4 solution over 5% Ni-WB_2, 10% Ni-WB_2, 15% Ni-WB_2, and 20% Ni-WB_2, respectively. All the polarization curves were obtained at a scan rate of 1 mV s^{-1} with 85% *i*R-compensations.

For comparison, we investigated the effect of different Ni doping amounts on the catalytic performance of WB_2. Specifically, When the amount of Ni doping increases to 10%, the activity is optimal. Then as the amount of Ni doping increases to 15% or even 20%, the activity decreases slightly. However, their catalytic activity is always better than undoped WB_2.
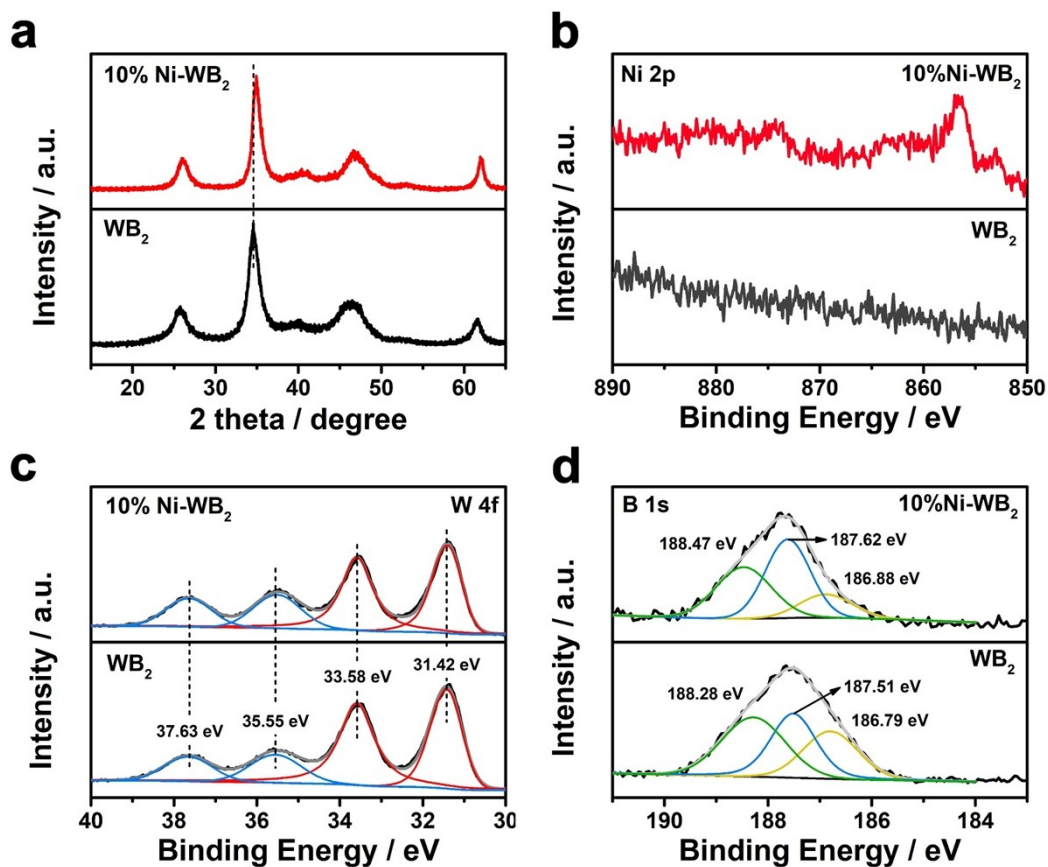
Fig. S7. (a) XRD pattern of WB_2 and 10% Ni-WB_2. High-resolution (b) Ni 2p, (c) W 4f, and (d) B 1s core level XPS spectra of WB_2 and 10% Ni-WB_2.

The XRD diffraction peaks of WB_2 and 10% Ni-WB_2 are similar, and their crystal structures are hexagonal (space group *p63/mmc*). Compared with WB_2, the peak position of 10% Ni-WB_2 is shifted to a high angle. According to the Bragg equation, this phenomenon indicates the contraction of its unit cell parameters, suggesting that Ni is doped into the WB_2 lattice. The radius of Ni is smaller than W, which causes the lattice constant to decrease and cell volume shrinkage. In addition, no new diffraction peaks appeared, indicating that 10% Ni-WB_2 still maintains the crystal structure of WB_2.
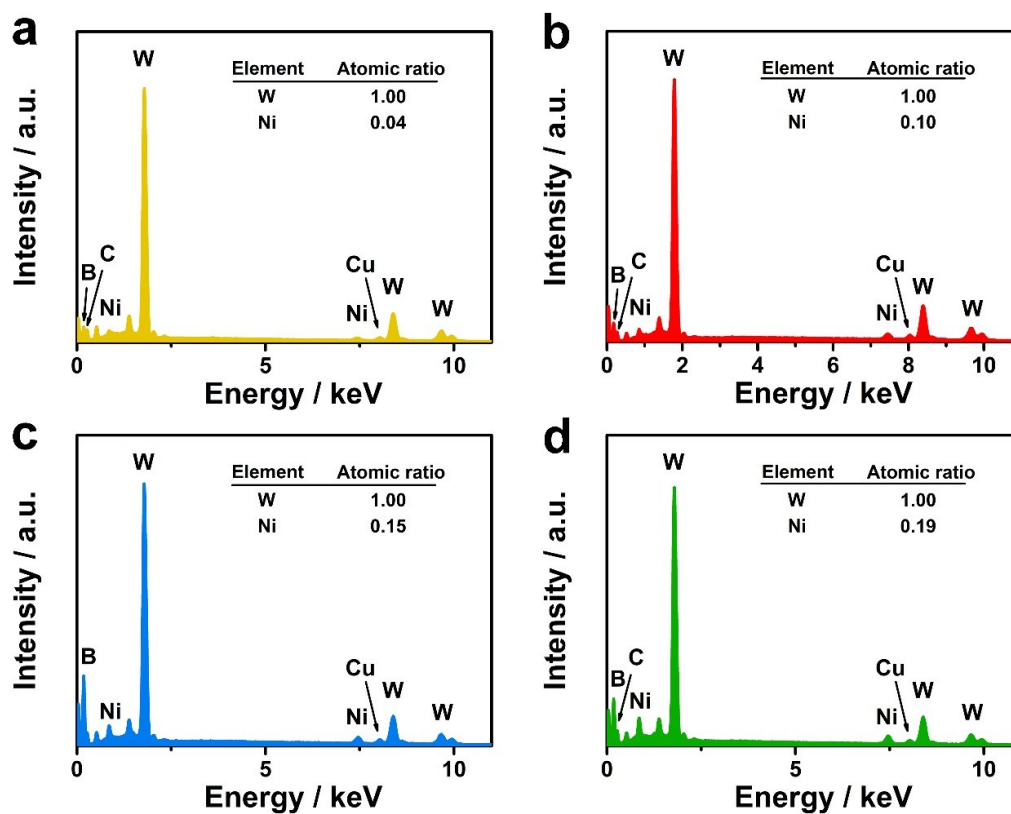
Fig. S8. Energy Dispersive Spectrum of (a) 5% Ni-WB$_2$, (b) 10% Ni-WB$_2$, (c) 15% Ni-WB$_2$, and (d) 20% Ni-WB$_2$.
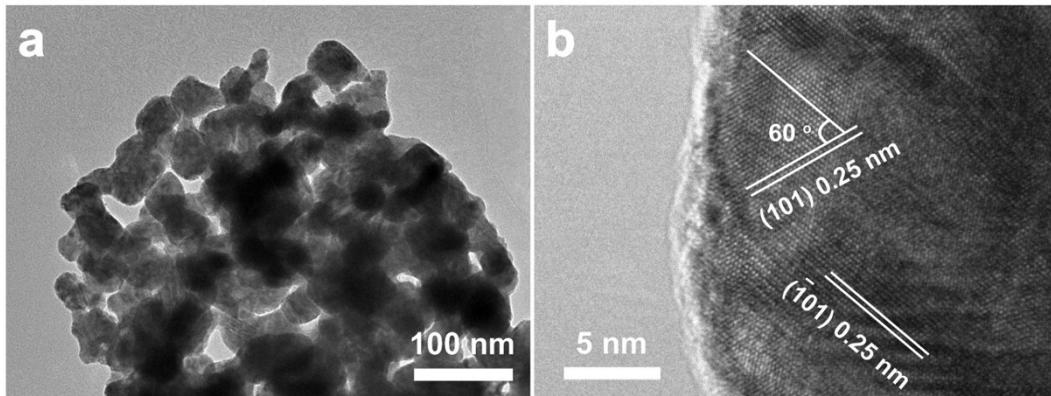
Fig. S9. (a) TEM and (b) HR-TEM images of 10% Ni-WB$_2$.

The TEM image of 10% Ni-WB$_2$ (Fig. S9a) indicates that the structure of 10% Ni-WB$_2$ and WB$_2$ is aggregated with particles having a particle size of less than 100 nm. The HR-TEM image (Fig. S9b) reveals that these nanoparticles have two set of lattice fringes with about 0.25 nm corresponding to the (101) atom planes of WB$_2$. The angle between them is 60°, which is in good agreement with the theoretical value. These results imply that the exposed facet in {001}. In addition, there are some stacking fault in 10% Ni-WB$_2$, which may be favorable in catalytic reaction due to their higher lattice energy.
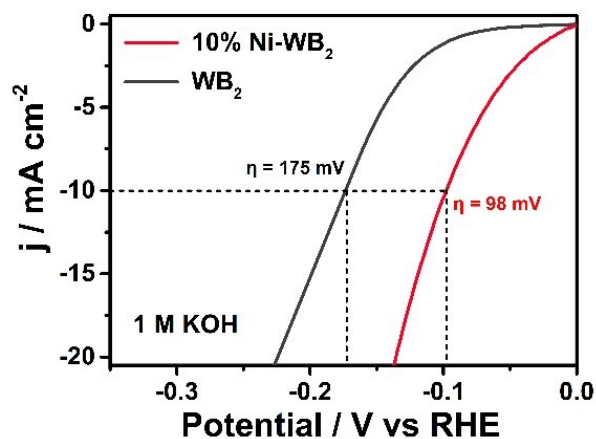
Fig. S10. Polarization curves of 10% Ni-WB$_2$ and WB$_2$ in 1M KOH electrolyte with 85% iR-compensations. The current densities are normalized by the geometric area.
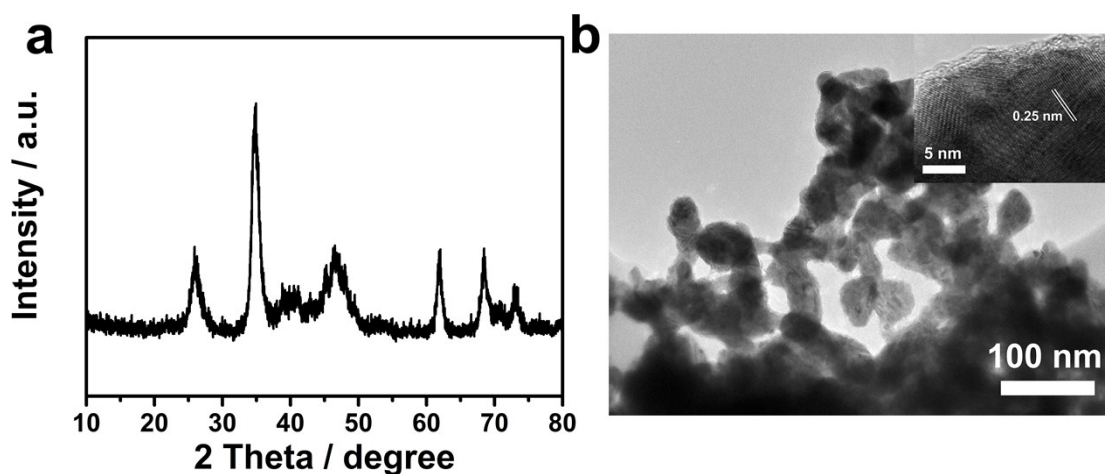
Fig. S11. (a) XRD, and (b) TEM and HR-TEM (insert) images of 10% Ni-WB$_2$ after 15 h durability test.

After the durability test, its surface components and morphology also remain unchanged, as manifested by the XRD, TEM and HRTEM characterization results.
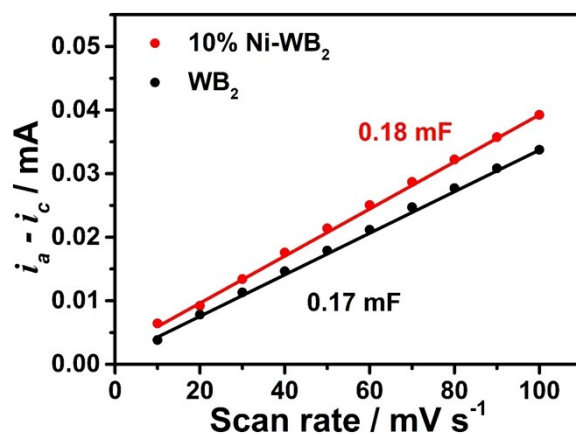
Fig. S12. The difference of between the anodic and cathodic currents plotted as a function of scan rate; the slope of the fitting line is used for determination of the double-layer capacitance (C_{dl}).
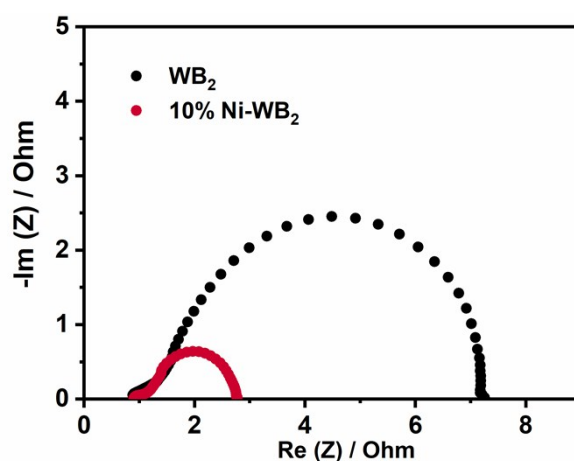
Fig. S13. Electrochemical impedance spectroscopy (ESI) Nyquist plots of 10% Ni-WB$_2$ and WB$_2$.

The electrochemical impedance spectroscopy is conducted for determining the interfacial electrode kinetics and the resistance of the material. The results reveal that 10% Ni-WB$_2$ has smaller R_{ct} values than WB$_2$, indicating that the electron transfer rates during HER is much faster in the presence of 10% Ni-WB$_2$.

2. Theoretical Section

2.1 Computation Details. All calculations were performed using the *Vienna Ab-initio Simulation Package* (VASP),[3,4] and the generalized gradient approximation (GGA) with the Perdew-Burke-Ernzerhof (PBE)[5] exchange-correlation functional was used with the projector augmented wave method.[6] For all theoretical models, the cutoff energy was 400 eV, the convergence threshold was set as 10^{-4} eV in energy and 0.02 eV Å^{-1} in force. The Brillouin zones were sampled by Monkhorst-Pack[7] $9 \times 9 \times 3$, $5 \times 9 \times 3$ and $5 \times 5 \times 1$ k-point grid for geometric optimization of bulk WB_2, bulk Ni doped WB_2 and slab models of them, respectively. For DOS of slab models, $7 \times 7 \times 1$ k-point grid was used. The symmetrization was switched off and the dipolar correction was included. The correction of van der Waals interaction was included using the DFT-D2 method.[8]

2.2 The Structure of WB_2 and Ni doped WB_2. Bulk WB_2 possesses hexagonal structure and its lattice belongs to the space group *P6$_3$/mmc*. After structure relaxation, the obtained lattice constants are a = 3.02 Å and c = 14.08 Å, which are close to the value of experiment (a = 2.987 Å and c = 13.895 Å).[9] The structure of WB_2 can be viewed as one graphene-like boron layer and one cyclohexane-like "chair" boron layer was alternately embedded in W metal framework (see Fig. S14a). There are four W atoms and eight B atoms in a unit cell. In the precious experiment study, we found that 10% Ni-WB_2 have the best activity and Ni was uniform distribution in WB_2 particles. Thus, we built $2 \times 1 \times 1$ supercell of WB_2 and replace one W atom with Ni atom (Ni-WB_2), which the percentage of Ni doping is 12.5% (see Fig. S14b). The lattice constants of Ni-WB_2 are a = 6.02 Å, b = 3.01 Å and c = 14.05 Å after structure relaxation, and α=β=91.01°, γ=120.02°. Compare with WB_2, the lattice constants of Ni-WB_2 become smaller and the lattice have some distortion, which caused by the smaller atomic radius of Ni atom (Ni = 149 pm *vs*. W = 193 pm).[10] We built the slab models of WB_2 and Ni-WB_2 with 2×2 and 1×2 repeated unit cell and eight atom layers, respectively. The 15 Å vacuum layer was selected to avoid inter-layer interactions. All the upper half of four

layers were fully relaxed and the remaining were kept frozen during computational process.

2.3 Computations of Free-Energy for the Hydrogen Evolution Reaction. The Gibbs free-energy of H^* (ΔG_{H*}) was calculated by the equation $\Delta G_{H*} = \Delta E_{H*} + \Delta ZPE - T\Delta S$, where ΔE_{H*}, ΔZPE and ΔS are as the adsorption energy, zero point energy and entropy change.[11] ΔZPE was obtained by $\Delta ZPE = ZPE\ (H^*) - 1/2\ ZPE\ (H_2)$, and in special, ΔS was obtained by $\Delta S = S\ (H^*) - 1/2\ S\ (H_2) \approx -1/2\ S\ (H_2)$ because of negligible vibrational entropy of H^*. At 298 K and 1 atm, $TS\ (H_2) = 0.41$ eV, thus $T\Delta S = -0.205$ eV.
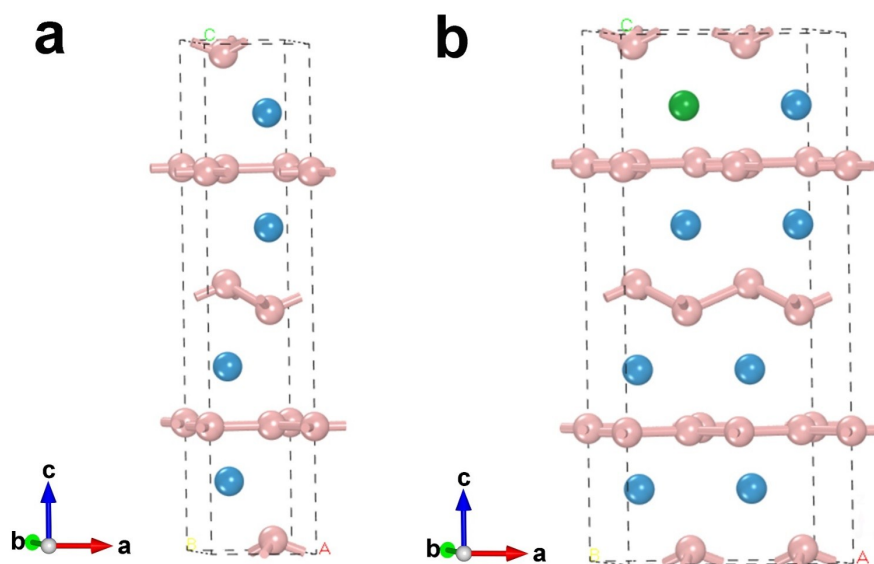
Fig. S14. (a) Crystal structure of WB_2 (Unit cell). (b) Crystal structure of Ni-WB_2 (2 × 1 × 1 supercell).
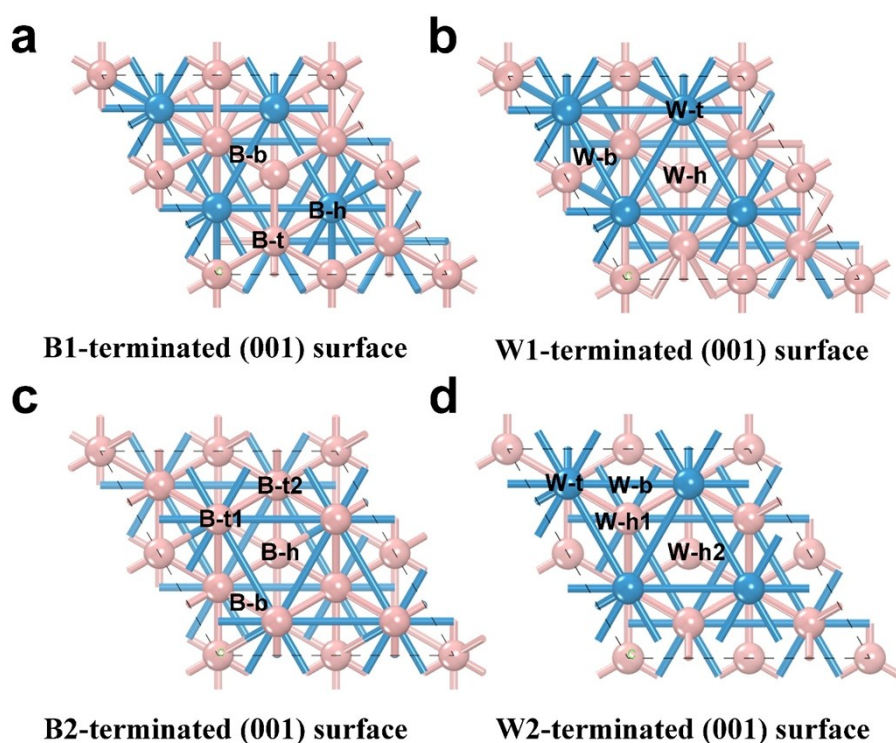
Fig. S15. The adsorption H* sites for WB_2 (001) surface in different terminations.

There are four types of (001) facets for WB_2 with different terminations: graphene-like boron layer termination denotes as B1-terminated (001) surface, cyclohexane-like "chair" boron termination as B2-terminated (001) surface, W layer bond to graphene-like boron layer denotes as W1-terminated (001) surface, W layer bond to cyclohexane-like "chair" boron denotes as W2-terminated (001) surface. Tab. S3-S6 show the ΔE_{H*} and ΔG_{H*} at different sites for different surface.

Tab. S3. The ΔE_{H*} and ΔG_{H*} at different sites (see Fig. S15a) for B1-terminated (001) surface of WB_2.

Sites	ΔE_{H*}	ΔG_{H*}
B-b	-0.70	-0.41
B-h	1.27	1.38
B-t	-0.57	-0.33

Tab. S4. The ΔE_{H^*} and ΔG_{H^*} at different sites (see Fig. S15b) for W1-terminated (001) surface of WB_2.

Sites	ΔE_{H^*}	ΔG_{H^*}
W-b	-0.85	-0.62
W-h	-0.88	-0.66
W-t	-0.65	-0.43

Tab. S5. The ΔE_{H^*} and ΔG_{H^*} at different sites (see Fig. S15c) for B2-terminated (001) surface of WB_2.

Sites	ΔE_{H^*}	ΔG_{H^*}
B-b	-1.30	-1.01
B-h	0.36	0.49
B-t1	-1.56	-1.26
B-t2	-0.13	0.07

Tab. S6. The ΔE_{H^*} and ΔG_{H^*} at different sites (see Fig. S15d) for W2-terminated (001) surface of WB_2.

Sites	ΔE_{H^*}	ΔG_{H^*}
W-b	Unstable	
W-h1	-1.11	-0.89
W-h2	-1.27	-1.01
W-t	0.10	0.27

B2-terminated (001) surface   **W2-terminated (001) surface**
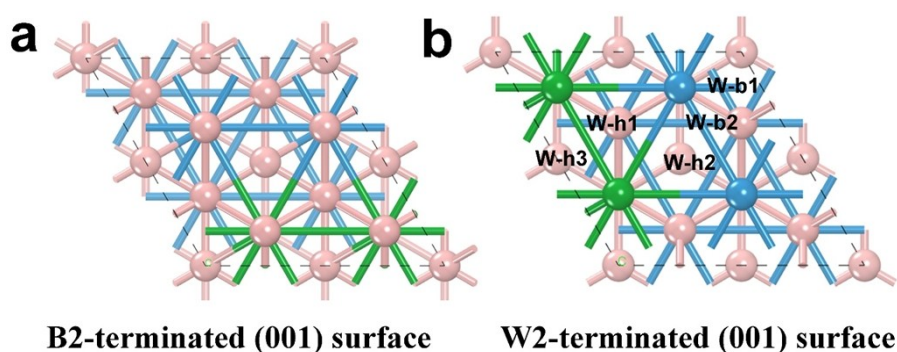
Fig. S16. The stable adsorption H* sites for Ni-WB$_2$ in different terminated.

There are also four type terminations for Ni-WB$_2$ (001) facets: graphene-like boron layer termination denotes as B1-terminated (001) surface, W layer bond to graphene-like boron layer denotes as W1-terminated (001) surface (see Fig. 4a, b); cyclohexane-like "chair" boron termination as B2-terminated (001) surface, W layer bond to cyclohexane-like "chair" boron denotes as W2-terminated (001) surface (see Fig. S16a, b). After structure relaxation, the obtained hydrogen adsorption configuration and the original surface boron layer of B2-terminated (001) are disorder. Thus, we only obtain the other three surfaces of ΔE_{H*} and ΔG_{H*} at different stable adsorption sites (See Tab. S7-S9).

Tab. S7. The ΔE_{H*} and ΔG_{H*} at different stable adsorption sites (see Fig. 4a) for B1-terminated (001) surface of Ni-WB$_2$.

Sites	ΔE_{H*}	ΔG_{H*}
B-b1	-0.57	-0.28
B-b2	-0.75	-0.43
B-b3	-0.21	0.08
B-b4	-0.54	-0.25
B-t1	-0.45	-0.21
B-t2	0.11	0.38
B-t3	-0.53	-0.28
B-t4	-0.07	0.21

Tab. S8. The ΔE_{H*} and ΔG_{H*} at different stable adsorption sites (see Fig. 4b) for W1-terminated (001) surface of Ni-WB$_2$ (001).

Sites	ΔE_{H*}	ΔG_{H*}
W-b	-1.29	-1.05
W-h1	-0.41	-0.24
W-h2	-0.46	-0.29
W-t	-0.89	-0.67

Tab. S9. The ΔE_{H*} and ΔG_{H*} at different stable adsorption sites (see Fig. S16b) for W2-terminated (001) surface of Ni-WB$_2$.

Sites	ΔE_{H*}	ΔG_{H*}
W-b1	-1.00	-0.80
W-b2	-1.32	-1.08
W-h1	-1.02	-0.82
W-h2	-1.31	-1.08
W-h3	-1.10	-0.88
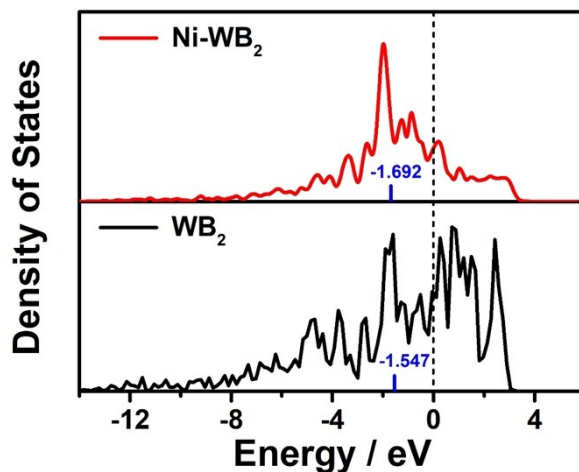
Fig. S17. The projected density of states of d-states in W1-terminated (001) surface for WB$_2$ and Ni-WB$_2$. The vertical line denotes the position of the Fermi energy, and blue bar indicate the d-band centers.

Fig. S17 present that their DOS crosses the Fermi level and exhibits metallic character. And the *d*-band center of Ni-WB$_2$ shifts from -1.55 eV to -1.69 eV compared with that of WB$_2$. This means more occupied in the antibonding states on W1-terminated (001) surface of Ni-WB$_2$, resulting in weaker H adsorption.

Tab. S10. The Bader charge of the top surface metal and boron atoms of B1-terminated (001) surface for WB$_2$ and Ni-WB$_2$ (The positive and negative value indicate lose electron and get electron).[12]

Charge	WB$_2$	Ni-WB$_2$
W	+1.04	+1.06
B	-0.30	-0.22
Ni	\	+0.10

Supplementary References

1. M. B. Stevens, L. J. Enman, A. S. Batchellor, M. R. Vise, A. E. Cosby, C. D. M. Trang and S. W. Boettcher, *Chem. Mater.,* 2016, **29**, 120.

2. D. Merki, H. Vrubel, L. Rovelli, S. Fierro and X. Hu, Chem. Sci., 2012, **3**, 2515.

3. J. P. Perdew, K. Burke and M. Ernzerhof, *Phys. Rev. Lett.*, 1996, **77**, 3865-3868.

4. P. E. Blöchl, *Phys. Rev. B*, 1994, **50**, 17953-17979.

5. G. Kresse and J. Furthmüller, *Comput. Mater. Sci.*, 1996, **6**, 15-50.

6. G. Kresse and J. Furthmüller, *Phys. Rev. B*, 1996, **54**, 11169-11186.

7. H. J. Monkhorst and J. D. Pack, *Phys. Rev. B*, 1976, **13**, 5188-5192.

8. S. Grimme, *J. Comp. Chem.*, 2006, **27**, 1787-1799.

9. C. Wang, Q. Tao, S. Ma, C. Tian, X. Wang, S. Dong and P. Zhu, *Phys. Chem. Chem. Phys.*, 2017, **19**, 8919-8924.

10. E. Clementi, D. L. Raimondi and W. P. Reinhardt, *J. Chem. Phys.*, 1967, **47**, 1300.

11. J. K. Nørskov, T. Bligaard, A. Logadottir, J. R. Kitchin, J. G. Chen, S. Pandelov and U. Stimming, *J. Electrochem. Soc.*, 2005, **152**, 23-26.

12. G. Henkelman, A. Arnaldsson and H. Jónsson, *Comput. Mater. Sci.*, 2006, **36**, 354-360.